



OPEN Active spiralling of microtubules driven by kinesin motors

Douglas Kagoiya Ng'ang'a¹, Samuel Macharia Kang'iri², Henry Hess³ & Takahiro Nitta¹✉

Cytoskeletal filaments propelled by surface-bound motor proteins can be viewed as active polymers, a class of active matter. When constraints are imposed on their movements, the propelled cytoskeletal filaments show dynamic patterns distinct from equilibrium conformations. Pinned at their leading ends, propelled microtubules or actin filaments form rotating spirals, whose shape is determined by the interplay between motor forces and the mechanics of the cytoskeletal filaments. We simulated the spiral formations of microtubules propelled by kinesin motors in an overdamped dynamics framework, which in addition to the mechanics of the spiralling microtubule explicitly includes the mechanics of kinesin motors. The simulation revealed that spiral formation was initiated by localized buckling of microtubules near the pinned ends, and the conditions for occurrence of spiral formation were summarized in a phase diagram. The radius of the formed spirals scaled with the surface motor density with an exponent of approximately $-1/4$, distinct from previous theoretical and simulation studies based on implicit modelling of motor proteins. This result can be understood as a consequence of the contributions of kinesin motors to the total elastic deformation energy, highlighting the importance of mechanics of motor proteins in the behaviour of the active polymers. These findings can be useful in accurate modelling of active polymers and in designing active polymer-based applications such as molecular shuttles driven by motor proteins.

Keywords Active polymer, Cytoskeletal filaments, Motor proteins, Computer simulation

Cytoskeletal filaments and their networks are active matters with remarkable mechanical properties, such as adaptation and remodelling, distinct from those of synthetic polymers^{1–3}. Such properties are mediated by active elements, such as motor proteins, as well as passive ones, such as binding proteins. A minimal reconstituted system to investigate emerging phenomena arising from interactions between cytoskeletal filaments and motor proteins is an *in vitro* motility assay^{4,5}, where the filaments are driven by motor proteins attached to a surface. Because of the activity of motor proteins, the cytoskeletal filaments are driven out of equilibrium and show distinct behaviours from those in thermal equilibrium. Cytoskeletal filaments driven by motor proteins can therefore be viewed as a type of active polymer, a class of active matter^{6,7}. Non-equilibrium phenomena exhibited by active matter include collective motions^{8–13}, transports¹⁴, motor-induced conformations¹⁵ and others. *In vitro* motility assays have also been developed into engineered systems, such as molecular shuttles^{16–21}, with applications in biosensing^{22–31}, computation³² and robotics^{33,34}.

Cytoskeletal filaments driven by surface bound motors show complex dynamical patterns, reminiscent of biological movements, when constraints are imposed on their movements. Microtubules (MTs) and actin filaments clamped at their leading ends and driven by surface-bound motors show flagellar-like beatings on the surface^{35–40}, which may serve as a minimal model to investigate the mechanism of flagellar beatings. Pinned at their leading ends, MTs or actin filaments form rotating spirals⁴¹, which are spatial-temporal patterns far from equilibrium. Bourdieu et al.⁴¹ derived a scaling relation for the spiral radius (R) against the motor density (σ): $R \propto \sigma^{-1/3}$ by balancing the bending moment of filaments with the torque produced by motors. Wang et al. performed Brownian dynamics simulations and obtained the same scaling relation⁴². The spiral formation is not only of scientific interest in spatio-temporal dynamic patterns^{7,35}, but also can be a limiting factor for efficient active transports in biosensors because sharp bending in the spirals can lead to the breaking of MTs and actin filaments^{43,44}.

Simulation studies investigating active polymers often use effective tangential force models⁷ where surface bound motors are implicitly included as effective tangential force along filaments and the mechanical properties of the motor proteins are overlooked. While effective tangential force models successfully reproduced the formation of active spiralling^{36,38,42}, it is unclear if the mechanical properties of the motors have an effect^{40,45}. Elastic linkers binding to the filaments are known to affect the conformations of cytoskeletal filaments. For

¹Applied Physics Course, Faculty of Engineering, Gifu University, 1-1 Yanagido, Gifu 501-1193, Japan. ²Department of Mechatronic Engineering, Dedan Kimathi University of Technology, 10100 Nyeri, Kenya. ³Department of Biomedical Engineering, Columbia University, New York, NY 10027, USA. ✉email: nitta.takahiro.y6@f.gifu-u.ac.jp

example, in living cells and in reconstituted systems, elastic linkers cause sinusoidal conformations of MTs, which are distinct from Euler buckling^{46–49}. Here, we use a simulation model of MTs propelled by kinesin-1 (hereafter, referred to as kinesin) motors, processive dimeric motors, which explicitly includes mechanical properties of the kinesin motor proteins^{50,51} and predict significantly different behaviours.

Results and discussion

Motility of pinned microtubules

In our simulations, MTs with lengths ranging from 5 to 30 μm were modelled as bead-rod polymers consisting of 10 to 60 segments with a rigidity equal to those of MTs (22.0 pN μm^2)⁵². The MT movement was simulated by solving overdamped equations of motion under the constraint of fixed segment length. Thermal fluctuations of MTs were not included unless otherwise mentioned in order to focus on the effects of the kinesin motors. The kinesin motors were modelled as active linear springs (spring constant of 100 pN/ μm)⁵³, with attachment points to the surface randomly distributed on the surface. If a MT segment comes within a 20 nm radius of the attachment point, the motor is assumed to bind to the MT and move towards the MT plus end with a force-dependent velocity (see Methods for details). While kinesin motors translocate on MTs in average around 1 μm before spontaneous dissociation,⁵⁴ to circumvent the complexity stemming from the spontaneous dissociation discussed in the section “Scaling argument of the spiral radius”, we assumed that kinesin motors translocate on MTs without dissociation unless a force larger than 7 pN⁵⁵ is exerted and focused on effects of mechanics of motor proteins on MT spiralling.

MTs were initially placed in straight conformations and allowed to move without pinning over a distance greater than their own length to reach a steady state. Subsequently, pinning was imposed at the leading ends of the MTs such that the leading ends were fixed in their positions and free to rotate as kinesin motors bound to the MTs continued moving towards the free (plus) end of the MT. Because the tails of the kinesin motors were adhered on the substrate, the kinesin motors push the MT towards the pinned end. This results in a compressive force that increases cumulatively towards the pinned end and leads to two distinct microtubule behaviours (Fig. 1). Figure 1a shows the MT conformation at 10 s and 5 s before pinning, and moments after pinning. In this case, the MT remains nearly in the conformation it was at the moment of pinning. Hereafter, we refer to this kind of motion as “stuck”. Figure 1b shows the movement of a MT undergoing a spiral formation. Immediately after pinning, the MT was observed to buckle in the plane of the surface, followed by pivoting around the pinned end at 5 s. Finally, the MT wound up around the pinned end forming a rotating section of a spiral starting at the pinning point followed by a roughly circular section at steady state.

The occurrence of the two types of movements depends on the length of MTs and the surface motor density as summarized in a phase diagram (Fig. 1c). Since outcomes were variable even for the same kinesin motor density and MT length due to the stochastic distribution of the motors on the surface, we performed multiple independent simulation runs for every point in the phase diagram and showed the fraction of spiralling that occurred. At low motor densities, short MTs occasionally detached from substrates. In such cases, we discarded the data and ran additional simulations to maintain the desired number of simulated MT movements remaining on surfaces for each condition. Spiralling tended to occur at high motor density and with long MTs while stuck behaviour tended to occur at low motor density and with short MTs.

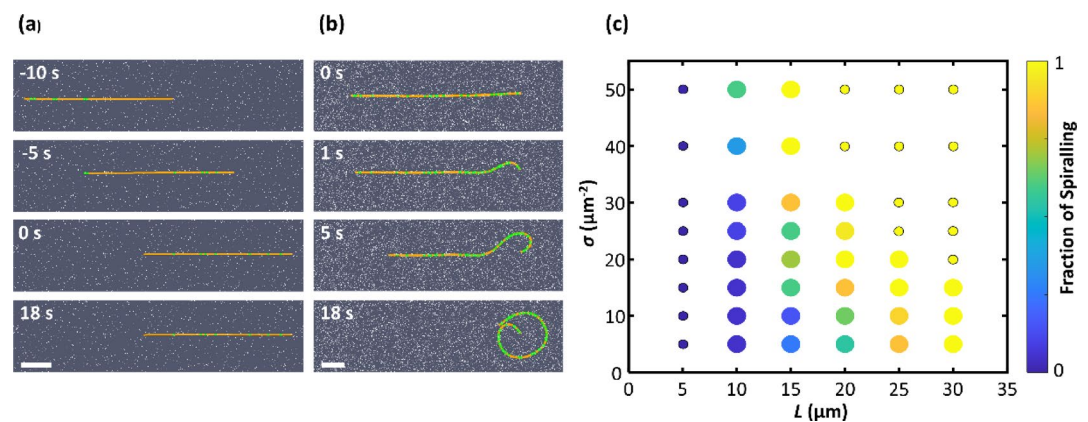


Fig. 1. Behaviours of kinesin motor-driven microtubules pinned at their leading ends. **(a, b)** Sequential images of a stuck **(a)** and spiral formation **(b)** of a microtubule (orange) driven by bound kinesin motors (green dots). The white dots represent randomly distributed kinesin motors. Pinning was imposed on the microtubules' leading ends (the right sides) at time of 0 s. The length of the microtubule is 10 μm ; the surface motor density is 10 μm^{-2} for **(a)**. See supplementary video 1. The length of the microtubule is 15 μm ; the surface motor density is 40 μm^{-2} for **(b)**. See supplementary video 2. Scale bars, 2 μm for both **(a)** and **(b)**. **(c)** Phase diagram of modes of microtubule movements. The size of each circle represents the number of simulation runs for each condition: large and small circles represent 20 and 5 simulation runs, respectively. The colour of the marks indicates the fraction of spiral that occurred: yellow indicates that all the microtubules formed spirals; dark blue indicates that no microtubules formed spirals.

Spiral formation and localized buckling

To investigate the formation of active spirals, we made detailed observations of MT movements. Figure 2a shows the time-evolution of a conformation of a pinned MT driven by kinesin motors. At the early stage of the time-evolution, localized buckling occurred near the MT pinned end. The amplitude of the localized buckling gradually increased while the horizontal length of the buckled regions stayed roughly the same, and the MT conformation eventually assumed a spiral shape. After reaching a steady state, the curvature of the MT along its contour was large near the pinned end and almost constant at the outer rim (Fig. 2b). The radius of the outer rim was measured (referred to as the spiral radius, R) by computing the radius of curvature of the plateau seen in the plot of the time averaged curvature as a function of the distance from its free end (s) at steady state (Fig. 2b). The spiral radius was independent of the MT length and decreased with the increase in the surface motor density as $R \propto \sigma^{-0.26 \pm 0.01}$ (Uncertainties of exponents in this study represent the standard deviations of the regressions) (Fig. 2c). This scaling relation differs from the theoretical prediction of $R \propto \sigma^{-1/3}$ obtained by Bourdieu et al.⁴¹ and simulation studies using effective tangential force models^{38,42}.

Since the localized buckling of MTs initiated the spiral formation, we closely investigated the localized buckling and measured the length of the localized buckling, l . For this, we looked at the curvature of MT along its contour at the moment that localized buckling occurred (Fig. 2d). The curvature as a function of the contour possessed at least two peaks, where the first and second peaks from the pinned end correspond to the crest and trough of the buckled MT, respectively. The distance between the second peak from the right side of a spline-interpolated curve and the pinned end of MT was measured as the localized buckling length. Measurements revealed that the localized buckling length followed a similar scaling relation with the spiral radius (Fig. 2c).

To investigate the cause of the localized buckling, we looked at bending energy of MTs and elastic energies of kinesin motors (Fig. 3a). Until the onset of the localized buckling, bound kinesin motors elongated as they moved

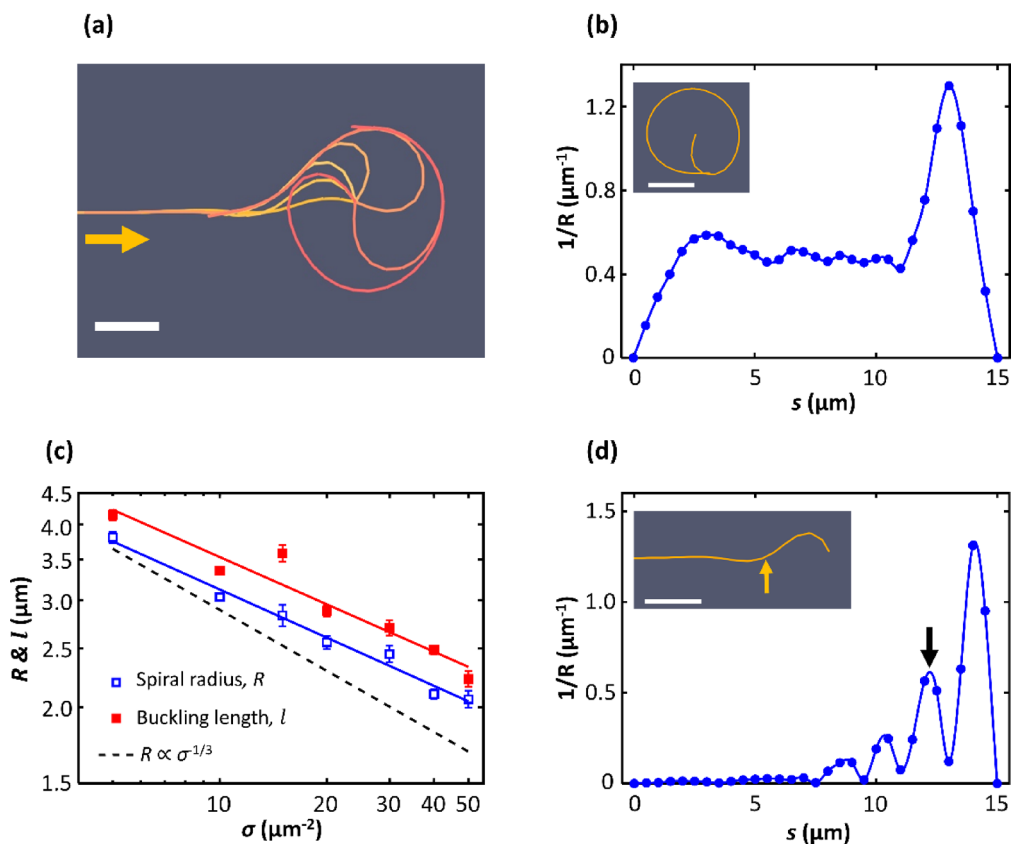


Fig. 2. Spiral formation and localized buckling. **(a)** A superimposed sequential image of a microtubule forming a spiral. The arrow points the direction of microtubule movement, and the colour change indicates time increase from orange to red. The length of the microtubule is 15 μm . The surface motor density is 20 μm^{-2} . **(b)** Curvature of a microtubule as a function of the distance from its free end (s) after forming a rotating spiral at a steady state. Inset, the snapshot of the microtubule conformation when the curvature is measured. **(c)** The spiral radius (R) and localized buckling length (l) vs. the surface motor density (σ). Open squares indicate the spiral radius; solid squares indicate the localized buckling length, (mean \pm S.D., $n = 5$). The solid lines are regressions of the data: $R \propto \sigma^{-0.26 \pm 0.01}$; $l \propto \sigma^{-0.26 \pm 0.03}$. The dotted line represents the scaling relation of $R \propto \sigma^{-1/3}$ for comparison. **(d)** Curvature of a microtubule as a function of the distance from its free end (s) at the onset of the localized buckling. The localized buckling length is the length from the pinned end to the point shown by the arrow. Inset, the snapshot of the microtubule conformation when the curvature is measured. Scale bars, 2 μm .

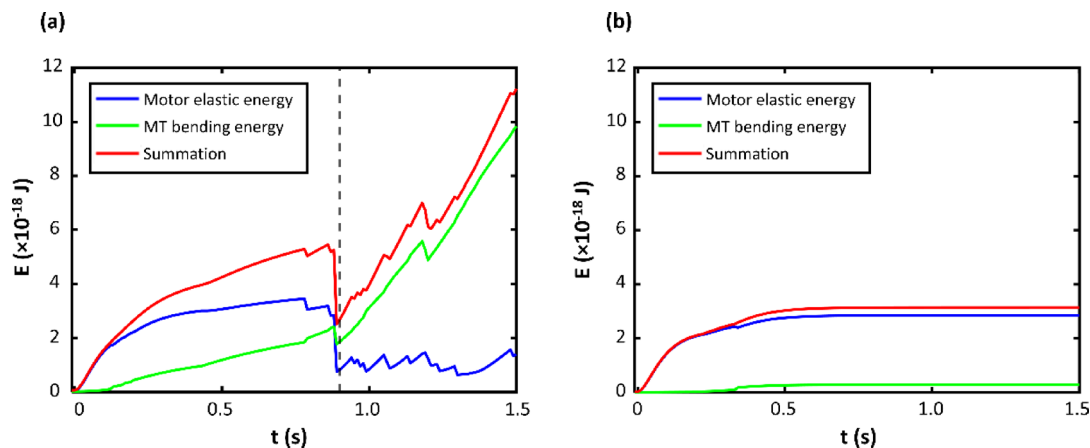


Fig. 3. The bending energy of microtubule and the elastic energy of kinesins binding to microtubules as function of time after pinning. The bending energy of the microtubule is shown in green; the elastic energy of kinesins binding to microtubules is shown in blue; the sum of the two is shown in red. **(a)** The time evolution of the three energies for a representative microtubule in the case of spiral formation. The broken black vertical line marks the time when localized buckling occurred. **(b)** The time evolution of the three energies for a representative stuck microtubule.

towards the free end of the MT, which caused the elastic energies of kinesin motors to increase. Meanwhile, the elastic energy of kinesin motors dominated the total elastic energy of the system, which is the sum of the bending energy of the MT and the elastic energies of the kinesin motors, and the MT maintained an almost straight conformation. At the onset of the localized buckling, the bending energy of the MT started to increase. Simultaneously, the elastic energies of kinesin motors decreased. The total elastic energy or the rate of its increase was decreased by the decrease in elastic energies of kinesin motors even though the bending energy of the MT increased. In the case of stuck microtubules, the elastic energies of kinesin motors dominated the total energy throughout the process and the bending energy of the MT remains low (Fig. 3b). These observations revealed that the elasticity of kinesin motors played a key role in the localized buckling of MTs.

Interestingly, the radius of the forming spiral is not determined by the buckling process. This is demonstrated by placing MTs into spiral conformations and observing their behaviour as they are propelled by the motors. If the spiral had a larger initial radius than that of a steady state spiral, the MT spiral contracted as the MT moved (Fig. 4a) and reached the steady state spiral radius for the given motor density after around 20 s (Fig. 4a). The radius of the MT spiral during contraction was calculated from the curvature profiles of each moment by taking an average of the segment curvature values at the outer rim. The outer rim region of the MT was determined by visual inspection. A closer look of the transition revealed that a part of the MT segment near the pinned end bulged out (Fig. 4b) and formed a new smaller spiral. Figure 4c shows how the radius of the spiral contracted and formed a new steady state spiral. The scaling relation of the new steady state spiral radius as a function of the surface motor density (Fig. 4d) was comparable to the scaling relation that was obtained when starting from a straight MT conformation (Fig. 2c). Furthermore, starting from spiral conformations, MTs can remain in spiral conformations even in the “stuck” phase in Fig. 1c (Supplementary Information Fig. S5), indicating that the occurrence of localized buckling is the limiting process for the spiral formation. If the spiral had a smaller initial radius than that of a steady state spiral, the MT spirals expanded (Fig. 4e) and reached the steady state spiral radius on the motor densities after around 20 s (Fig. 4c). The radius of the MT spiral during expansion and at steady state was calculated using the same method as that of contracting spiral. Expansion occurred only around the region of the semicircular arc associated with the pinned end (Fig. 4f). Figure 4g shows how the radius of the spiral expanded and formed a new steady state spiral as time changed. We then obtained the new steady state spiral radius as a function of the surface motor density (Fig. 4h). The scaling relation was again comparable to the scaling relation that was obtained by when starting from a straight MT conformation (Fig. 2c). The steady state spiral radius at low motor density showed deviations from that of MTs that started from straight conformation (Fig. 4h). Presumably, these deviations resulted from pronounced fluctuations of MT conformations at low motor density even in spiralling at their steady state (Supplementary Information, Fig. S6). Overall, these observations showed that the occurrence of localized buckling is the limiting process for the spiral formation and that the spiral radius has its stable steady state value regardless of the MT initial conformation once a spiral is initiated.

Mechanism of localized buckling and phase diagram

The phase diagram of microtubule behaviour as function of motor density and microtubule length (Fig. 1c) can be explained with the theory of elasticity based on the observations that localized buckling initiated the spiral formation and that the elasticity of kinesin motors played a key role. The effect of linker elasticity on the deformation of a semiflexible polymer subjected to compressive force at both ends has been studied previously^{46,47}. A detailed account of the analytical theory is given in Supplementary Information “Effects of

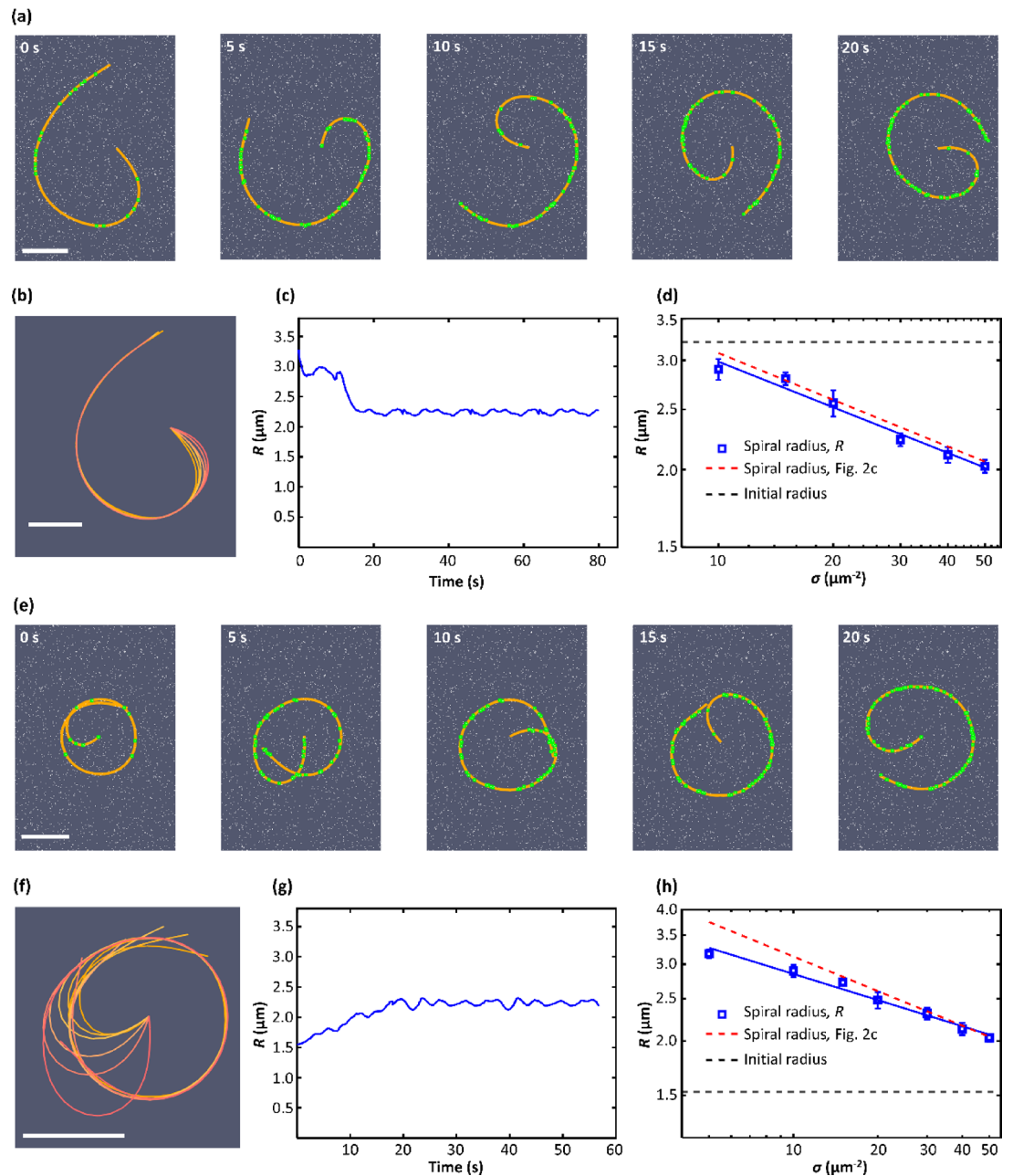


Fig. 4. (a) Sequential images of a contraction of a microtubule spiral with a larger initial radius than that at the steady state shown in Fig. 2c. The microtubule is represented in orange; kinesin motors are represented with white dots; bound kinesin motors are highlighted with green dots. The length of the microtubule is $15\ \mu\text{m}$. The motor density is $30\ \mu\text{m}^{-2}$. See supplementary video 3. (b) Superimposed microtubule conformations within the first 1.0 s. The colour changes from yellow to red represents the change in time. (c) The time evolution of the spiral radius during the contraction process. (d) The spiral radius (R) vs. the surface motor density (σ), (mean \pm S.D., $n = 5$). The solid line is a regression of the data: $R \propto \sigma^{-0.24 \pm 0.02}$. The initial spiral radius is indicated with the black broken line. The regression of the spiral radius at the steady state in Fig. 2c is shown with the red broken line for comparison. (e) Sequential images of the expansion of a microtubule spiral with a smaller initial radius than that at the steady state shown in Fig. 2c. The microtubule is represented in orange; kinesin motors are represented with white dots; bound kinesin motors are highlighted with green dots. The length of the microtubule is $15\ \mu\text{m}$. The surface motor density is $30\ \mu\text{m}^{-2}$. See supplementary video 4. (f) Superimposed microtubule conformations within the first 1.0 s. The colour changes from yellow to red represent the change in time. (g) The time evolution of the spiral radius during the expansion process. (h) The spiral radius (R) vs. the surface motor density (σ), (mean \pm S.D., $n = 5$). The solid line is a regression of the data: $R \propto \sigma^{-0.20 \pm 0.01}$. The initial spiral radius is indicated with the black broken line. The regression of the spiral radius at the steady state in Fig. 2c is shown with the red broken line for comparison. Scale bars, $2\ \mu\text{m}$.

elastic links on microtubule conformation⁷. Semiflexible polymers with bending modulus κ embedded in an elastic medium with effective elastic modulus α and subjected to a force F at both ends remain straight up to $F_c = \sqrt{4\alpha\kappa}$, and undergo buckling at F_c with a wavelength of $2\pi\left(\frac{\kappa}{\alpha}\right)^{1/4}$, provided the polymer is longer than the half wavelength^{46,56}. The predicted conformations agreed with sinusoidal MT conformations in living cells and in reconstituted systems^{46–49}. These theoretical results do not apply in a straightforward manner to the localized buckling of MTs, because the force exerted on MT segments by the kinesin motors is not constant along MTs.

For the localized buckling of MTs, the forces of the kinesin motors combine to increase the force acting on the MT segments towards the pinned end (Fig. 5a). The force profile can be approximated as $2f(t)\sigma ws$, where $f(t)$ is the magnitude of force generated by a single kinesin motor; σ is the motor density; w is the effective reach of kinesin motors; and s is the distance from the MT free end. $f(t)$ is an increasing function of time and becomes levelled-off with the magnitude of the stall force of kinesin motors (f_{stall}) because, as the kinesin head moves along the MT towards the free end, the force exerted by the kinesin increases until it stalls (Fig. 5a). As the maximal force at the tip increases, the compressive force will reach the critical force $F_c = \sqrt{4\alpha\kappa}$ at time t_2 and then exceed it, but the length of the region where $F > F_c$ is shorter than the half wavelength of $\pi\left(\frac{\kappa}{\alpha}\right)^{1/4}$, so that localized buckling does not occur. Only at a later time t_3 will the length of the region where $F > F_c$ exceed the half wavelength, and the MT will undergo buckling near the pinned end with the localized buckling length of $\pi\left(\frac{\kappa}{\alpha}\right)^{1/4}$. The maximum value of $f(t)$ is limited by the stall force of the kinesin motors. When the increase of the slope of the force profile is terminated before the length of the region where $F > F_c$ exceeds the half wavelength, the MT remains in a straight conformation, that is, the MT is stuck.

The predicted length of localized buckling is an approximation, because the boundary conditions in the theory are different from those in the simulation. In the theory, both ends of a localized buckling region are fixed in their locations and free to rotate. In contrast, in the simulation, the pinned end is fixed in location and free to rotate; the other end of a localized buckling region is neither fixed in location nor free to rotate.

The above scenario, (Fig. 5a), of the occurrence of localized buckling based on the elastic foundation theory predicts that the length of the localized buckling is comparable with $\pi\left(\frac{\kappa}{\alpha}\right)^{1/4}$. Since $\alpha = 2k\sigma w$ ^{47,57} where k is the spring constant of kinesin motors, the length of localized buckling scales with $\sigma^{-1/4}$, which is in agreement with our simulation result (Fig. 5b). The prediction is also consistent with our observation that the localized buckling length is independent of the length of the MTs.

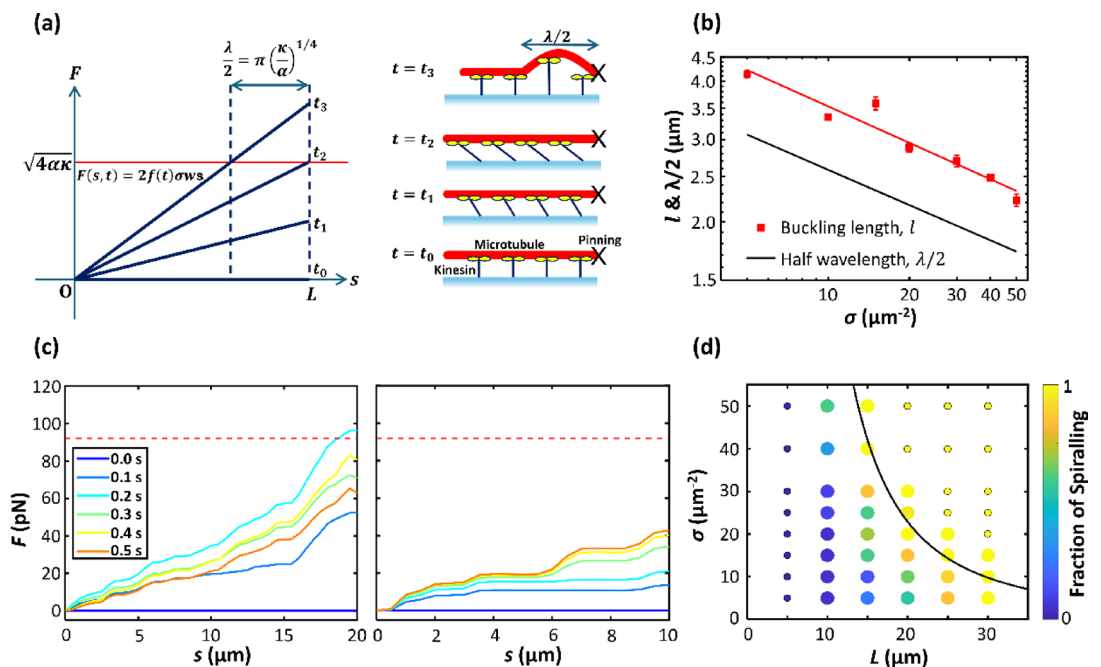


Fig. 5. (a) A schematic of the mechanism of localized buckling. The left side shows the compressive force profile at four times (t_0 to t_3). The right side shows the corresponding schematic drawings of the microtubule and kinesins at time from t_0 to t_3 . (b) The comparison between localized buckling length obtained from the simulations (red solid squares; the red solid line represents the regression line: $l \propto \sigma^{-0.26 \pm 0.03}$) and the half wavelength calculated from the elastic theory (black solid line), (mean \pm S.D., $n = 5$). (c) Compression force as a function of the distance from the free end for a 20 μm long buckling MT (left), and 10 μm long stuck MT (right), with equal surface motor density of $20 \mu\text{m}^{-2}$ at different times after pinning. The localized buckling occurred at 0.2 s. The red broken lines show the calculated critical buckling force. (d) Phase diagram of modes of microtubule movements with the theoretical boundary curve (black curve).

The scenario illustrated in Fig. 5a can be directly compared with the results of our computer simulations. For the case of buckling MTs, when the compression force exerted by kinesin motors on MT segments reaches the critical value near the pinned ends, the compression force would decrease due to the localized buckling of MTs causing a release of tension within individual kinesin motors. The simulation results qualitatively agree with the scenario (Fig. 5c left). In many cases, the force profiles appeared to start to decrease before the length of the region where $F > F_c$ exceeds the half wavelength. This is presumably caused by undulated conformations of MTs which promote buckling. For the cases of stuck MTs, the force increased toward MT's pinned ends. The slope of the force profile initially increased with time and then saturated (Fig. 5c right).

Another prediction from the scenario shown in Fig. 5a relates to the boundary of the two phases in the phase diagram. For the localized buckling and hence spiralling to occur, the force profile must have regions of $F > F_c$ longer than the half wavelength. This means that the force profile $F(s, t)$ in Fig. 5a reaches $F_c = \sqrt{4\alpha\kappa}$ at $s = L - \pi \left(\frac{\kappa}{\alpha}\right)^{1/4}$. Because the maximum of $f(t)$ is f_{stall} , the boundary curve relating motor density and MT length is thus defined by the condition:

$$\sqrt{4\alpha\kappa} = 2f_{stall}\sigma w \left[L - \pi \left(\frac{\kappa}{\alpha}\right)^{1/4} \right]. \quad (1)$$

The value of w was determined to be 24 nm by analysing simulation results (Supplementary Information, Estimation of effective reach, w). The boundary curve qualitatively reproduced the phase boundary in Fig. 5d, but spiralling already can occur in the simulations at lower lengths and motor densities. We attribute this to not fully straight MT conformations at the moment of pinning, which promote buckling. This is supported by simulations including thermal fluctuations. The addition of thermal fluctuations to the simulation of the motion of the MT segments further promotes buckling by pre-bending the MTs (Fig. 6). However, while the boundary between buckling and getting stuck shifts, the shape of the boundary curve remains similar.

Scaling argument of the spiral radius

A mechanistic explanation is required as to why the spiral radius is proportional to $(\kappa/\alpha)^{1/4}$ and how the steady state spiral radius is achieved when MTs movements started from either expanded or compacted spirals (Fig. 4). To account for the contraction or expansion of spirals shown in Fig. 4, the scenario (Fig. 5a) cannot be used because it considers infinitesimal deformations from initial straight conformations. Therefore, we make a

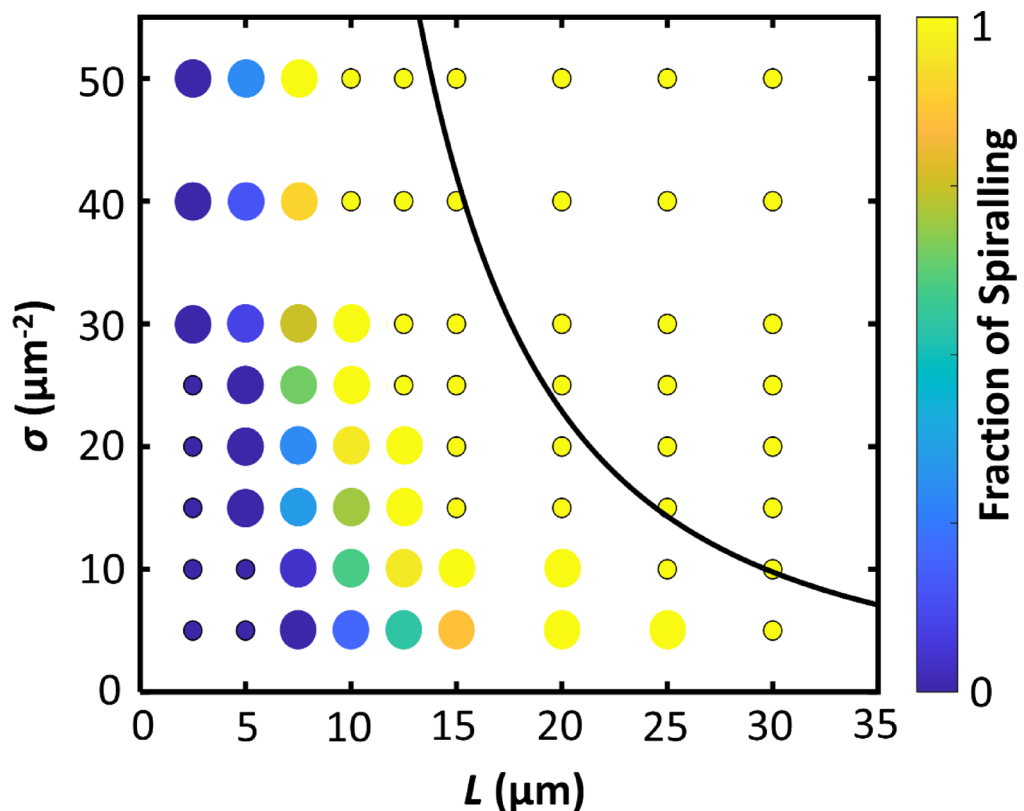


Fig. 6. Phase diagram of microtubule movements with thermal fluctuations. The size of each circle represents the number of simulation runs for each condition: large and small circles represent 20 and 5 simulation runs, respectively. The colour of the marks indicates the occurrence of outcome. The curve indicates the theoretical boundary curve.

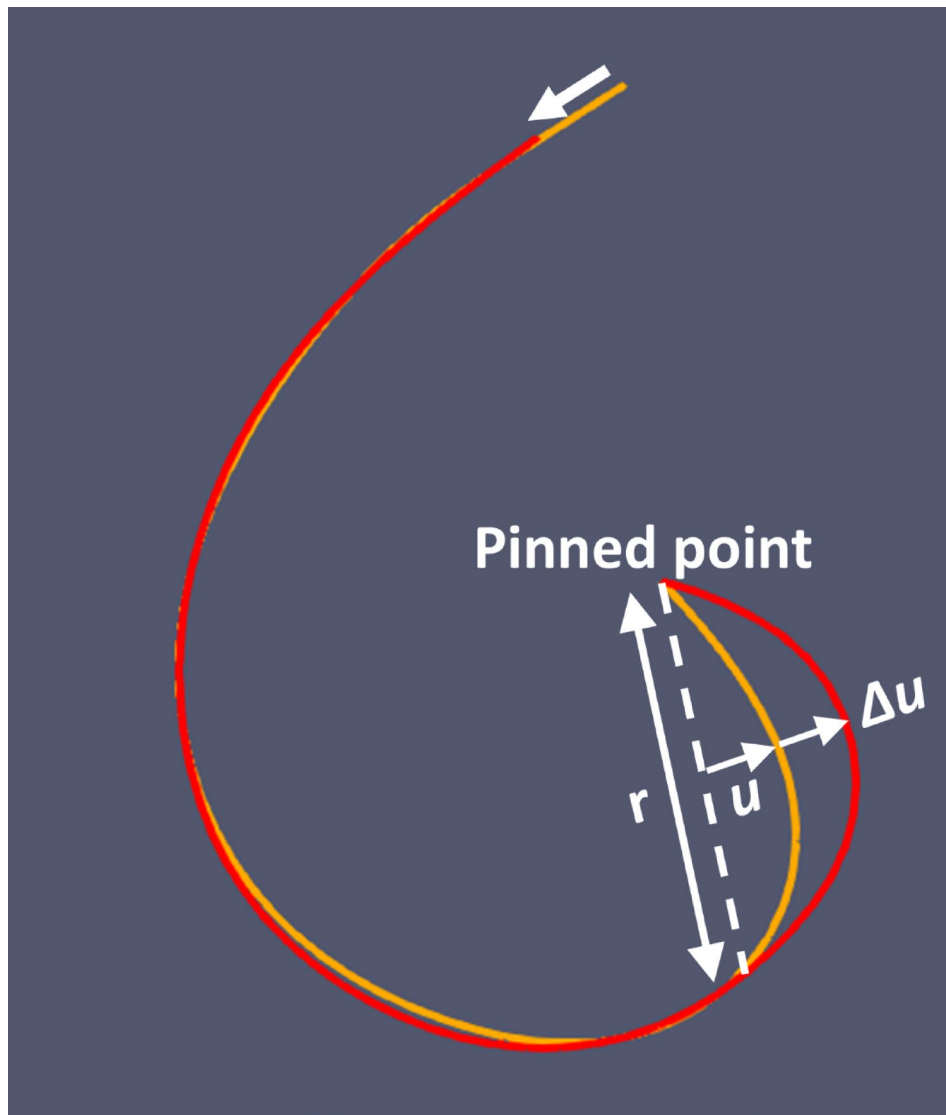


Fig. 7. A schematic representation of the scaling argument. The orange curve shows an initial microtubule conformation. The red one shows a microtubule conformation after a displacement of Δu . The length of the bulging regions is denoted by r .

scaling argument as follows (Fig. 7). The scaling argument is based on our observations that the changes in MT conformations were initiated in regions of MTs near their pinned ends (Fig. 4b and f) and that the length of these regions of the MTs, denoted by r , evolved into the steady-state spiral radius after expansion or contraction. Because the other part of MT conformations remained almost the same, we assumed that the dominant changes in MT bending and kinesin elastic energy occurred in the regions near the pinned ends. When the region of a MT makes a lateral displacement of Δu from an initial curved conformation described with u (Fig. 7), this causes the changes in the bending of the MT and elongations of kinesin motors binding on the region of the MT. The MT curvature changes from u/r^2 to $(u + \Delta u)/r^2$, so that the change in the bending energy of the MT scales as $\sim \kappa \Delta u \cdot r^{-3}$. In addition, as the change in the elongations of kinesin motors is $\sim \Delta u$ and the number of stretched kinesin motors is proportional to r , the change in the summation of the elastic energy of binding kinesin motors scale as $(1/2) \alpha (\Delta u)^2 r$. Thus, the increase of the energy of the system consisting of the MT and the kinesin motors, ΔE , is $\sim \kappa \Delta u \cdot r^{-3} + (1/2) \alpha (\Delta u)^2 r$. Since we assumed an overdamped system, the change in the MT curvature must occur at the value of r that gives the minimum ΔE . This leads to $r \propto (\kappa/\alpha)^{1/4}$. This scaling relation agrees with the simulation result in Figs. 2c and 4d and h.

Freely jointed chain models, which are nonlinear spring models, have been used in modelling kinesin motors^{58,59}. While the freely jointed chain models can be more accurate than the linear spring model for highly stretched motors, we used the linear spring model for simplicity. However, since our scaling arguments rely on infinitesimal displacements of MTs, corresponding to infinitesimal elongations of kinesin motors, the arguments remain valid even when nonlinear spring models of kinesin motors are considered. This is because localized buckling and bulging occur before kinesin motors are significantly stretched where nonlinear elastic effects

become pronounced. Hence, any potential influence of nonlinearity of motor mechanics on the formation and size of the spirals would be marginal. In addition, the stretch of simulated kinesin motors bound to the outer rims of the MT spirals at steady state was approximately 24 nm (Supplementary Information, Fig. S7), which is about one-third of the contour length of a full-length kinesin-1 molecule. Hence, modelling kinesin motors as linear springs is reasonable for the purposes of this study.

A scaling relation between the spiral radius and motor density has been derived by Bourdieu et al.⁴¹: $R \propto \sigma^{-1/3}$. Their scaling argument was based on the balance between the torque generated by binding motors and the bending moment of the filament and did not take into account the elasticity of motor proteins. The scaling exponent of $-1/3$ by Bourdieu et al. showed agreement with the experimental data for an actomyosin motility assay⁴¹. We surmise that the agreement between their theoretical and experimental scaling exponents stems from the low duty ratio of the motor proteins used in the experiment. Bourdieu et al. used non-processive myosin II motors, which bind actin filaments for only about 5% of their chemomechanical cycle. The low processivity of myosin II motors can lead to unbinding of stretched binding motors and to bindings of unstretched or less stretched ones during formation of spirals, providing another pathway to release the elastic energy of motors. As a result, the elastic energy of myosin II motors cannot build up over time, thus having little contribution compared with the bending energy of actin filaments. This would be the reason why the scaling relation ignoring the elastic contributions of motor proteins agreed with the experimental data for the actomyosin motility assay. Our study is complementary to the study by Bourdieu et al.⁴¹ in that we investigated an active polymer system driven by motors with high duty ratio. While we are not aware of an experiment obtaining a scaling exponent between the spiral radius and motor density other than the actin/myosin systems, our simulation study predicts that the exponent of $-1/4$ can be experimentally observed in kinesin/MT systems. In experiments, due to the finite run length of kinesin motors, an intermediate value between $-1/3$ and $-1/4$ may be observed.

Conclusions

Using computer simulations of MTs propelled by kinesin motors, which explicitly include the mechanical properties of kinesin motors, we investigated active spiralling of pinned MTs. We found either stuck MTs or spiralling MTs, depending on the MT length and surface motor density, and summarized the findings in a phase diagram. In addition, we found that the spiral radius followed a scaling relation against the motor density distinct from that of previous studies. These findings were elucidated by taking into account the mechanical property of kinesin motors, highlighting the importance of explicitly including the mechanics of motor proteins in computer simulations.

Our results also show that, while semiflexible polymers driven by surface bound motors and active polymers consisting of active particles, such as Janus particles, qualitatively behave in similar manners, their behaviours could be different in the details. The difference may affect the overall performance of applications integrated with active polymers.

Another insight obtained from this study is that as spirals with small radius can cause breakage of MTs⁴⁴, the use of a low motor density would be beneficial to prevent breakages of molecular shuttles. Finally, this study may provide an insight into elementary processes of active interactions between cytoskeletal filaments and motor proteins in living cells.

Simulation methods

The simulation method was based on our previous work^{50,51}. In the following, we briefly summarize the simulation method. We assumed the MTs to be infinitely thin and inextensible semiflexible bead-rod polymers with a flexural rigidity of 22.0 pN μm^2 (ref.⁵²). The length of MTs was set to be from 5 to 30 μm and each MT consisted of 10 to 60 rigid segments depending on the length of MTs. MT movement was simulated by solving overdamped equations of motion under the constraint of fixed segment length. Thermal fluctuations were not included unless otherwise mentioned.

In this method, a single time step consisted of the following two steps.

In the first step, the beads representing an MT were moved without considering any constraint, using the following expression:

$$\mathbf{r}'_i(t + \Delta t) = \mathbf{r}_i(t) + \frac{\Delta t}{\zeta} \mathbf{F}^{bending,i} + \frac{\Delta t}{\zeta} \mathbf{F}^{kinesin,i}, \quad (2)$$

where \mathbf{r}_i is the position vector of the i -th bead consisting of a MT, ζ is the viscous drag coefficient, $\mathbf{F}^{bending,i}$ is the restoring force of MT bending, $\mathbf{F}^{kinesin,i}$ is a force exerted by bound kinesins. Δt was set at 0.5×10^{-6} s to ensure numerical stability. The viscous drag coefficient used was the average of the parallel and perpendicular drag coefficients⁶⁰:

$$\zeta = \frac{3\pi \eta d}{\ln\left(\frac{d}{2r}\right)} \quad (3)$$

where η is the viscosity of water (0.001 Pa s), d is the length of the MT segment (0.25–0.50 μm), and r was the radius of MT (12.5 nm). We chose this length of the MT segmentation such that taking shorter MT segmentation leads to negligible change of results (Fig. S4).

In case of simulating movements of MTs subjected to thermal fluctuations (Fig. 6), the Eq. (2) was replaced by:

$$\mathbf{r}'_i(t + \Delta t) = \mathbf{r}_i(t) + \frac{\Delta t}{\zeta} \mathbf{F}_{bending,i} + \frac{\Delta t}{\zeta} \mathbf{F}_{kinesin,i} + \sqrt{2D \cdot \Delta t} \boldsymbol{\xi}_i, \quad (4)$$

where D is the diffusion coefficient of the bead calculated as $D = k_B T / \zeta$.

The restoring force of MT bending was calculated from the following bending potential⁶⁰:

$$U = \frac{1}{2} \frac{\kappa}{d^3} \sum_{i=2}^{n-1} (\mathbf{r}_{i+1} - 2\mathbf{r}_i + \mathbf{r}_{i-1})^2 \quad (5)$$

where κ is the flexural rigidity.

Kinesin motors were randomly distributed over the allowed surface by specifying the positions of the kinesin tails. If an MT segment came close to a kinesin motor tail within a capture radius (20 nm)⁵⁷, the kinesin motor was assumed to be bound to the MT segment, and the position of the motor head was specified on the MT segment. Once bound, the head of the bound kinesin motor moved toward the MT plus end with a force-dependent velocity expressed as

$$v(F_{\parallel}) = v_0 \left(1 - \frac{F_{\parallel}}{F_{stall}} \right) \quad (6)$$

where v_0 is the translational velocity without applied force, F_{\parallel} is the component of the pulling force along the MT, and F_{stall} is the stall force of the kinesin motors. v_0 was set at 0.8 $\mu\text{m/s}$, and F_{stall} was set at 5 pN. The bound kinesin acted as a linear spring between the motor head and tail with the spring constant of 100 pN/ μm ⁵³ and with an equilibrium length of zero and exerted a pulling force on the MT segment. The pulling force was divided into two forces which acted on the two beads located at either end of the MT segment where the kinesin motor was bound, under the condition that the total force and torque on the segment remained the same. A kinesin motor bound to an MT detached when tension reached 7 pN⁵⁵. The choice of the spring constant and the detachment force leads to the maximum stretch of 70 nm, which is close to the contour length of kinesin motors⁶¹. By following the approach taken by Gibbons et al.,⁶² we neglected the spontaneous dissociation of the bound kinesin from the MT.

In dealing with Eq. (2), we used an implicit-explicit method, where the restoring force of MT bending was implicitly calculated while other terms were explicitly calculated.

In the second step, the unconstrained movements were corrected by considering the constraints due to the segment length and the guiding tracks. To keep the segment length constant, the coordinates of the beads representing the MT $\{\mathbf{r}_i\}$ as shown were subject to the following holonomic constraints:

$$g_{segment,k} = (\mathbf{r}_{k+1} - \mathbf{r}_k)^2 - d^2 = 0 \quad (k = 1, \dots, n-1) \quad (7)$$

In addition, to keep the MT movement above the substrate, the position of the beads representing the MT were subjected to the following holonomic constraints:

$$g_{track,i} = z_i = 0, \text{ if } z_i < 0 \quad (8)$$

The correction was carried out with the following expression:

$$\mathbf{r}_i(t + \Delta t) = \mathbf{r}'_i(t + \Delta t) + \Delta \mathbf{r}_i(t + \Delta t) \quad (9)$$

where $\Delta \mathbf{r}_i(t + \Delta t)$ is the correction term

$$\Delta \mathbf{r}_i(t + \Delta t) = \frac{\Delta t}{\zeta} \sum_{k=1}^{n-1} \lambda_{segment,k} \frac{\partial g_{segment,k}}{\partial \mathbf{r}_i} + \frac{\Delta t}{\zeta} \lambda_{track,i} \frac{\partial g_{track,i}}{\partial \mathbf{r}_i} \quad (10)$$

and $\lambda_{segment,k}$ and $\lambda_{track,i}$ are Lagrangian multipliers, which were determined in order for the coordinate at $t + \Delta t$ to satisfy the constraints given by Eqs. (7) and (8), respectively. For this, we went through the calculations for the constraints one by one, cyclically, adjusting the coordinates until the constraints were satisfied with a tolerance of 10^{-6} μm .

To impose the pinning at MT leading end, the position of the bead located at the MT leading end was fixed allowing free rotations around it.

Simulation results were visualized with ParaView (<https://www.paraview.org/>).

Data availability

The datasets generated during and/or analysed during the current study are available from the corresponding author on reasonable request.

Received: 25 February 2025; Accepted: 20 May 2025

Published online: 01 July 2025

References

- Fletcher, D. A. & Mullins, R. D. Cell mechanics and the cytoskeleton. *Nature* **463**, 485–492 (2010).
- Burla, F., Mulla, Y., Vos, B. E., Auferhorst-Roberts, A. & Koenderink, G. H. From mechanical resilience to active material properties in biopolymer networks. *Nat. Rev. Phys.* **1**, 249–263 (2019).
- Needleman, D. & Dogic, Z. Active matter at the interface between materials science and cell biology. *Nat. Rev. Mater.* **2**, 17048 (2017).
- Kron, S. J. & Spudich, J. A. Fluorescent actin filaments move on myosin fixed to a glass surface. *Proc. Natl. Acad. Sci. USA*. **83**, 6272–6276 (1986).
- Howard, J., Hudspeth, A. J. & Vale, R. D. Movement of microtubules by single kinesin molecules. *Nature* **342**, 154–158 (1989).
- Winkler, R. G., Elgeti, J. & Gompper, G. Active polymers—emergent conformational and dynamical properties: A brief review. *J. Phys. Soc. Jpn.* **86**, 101014 (2017).
- Winkler, R. G. & Gompper, G. The physics of active polymers and filaments. *J. Chem. Phys.* **153**, 040901 (2020).
- Schaller, V., Weber, C., Semmrich, C., Frey, E. & Bausch, A. R. Polar patterns of driven filaments. *Nature* **467**, 73–77 (2010).
- Sumino, Y. et al. Large-scale vortex lattice emerging from collectively moving microtubules. *Nature* **483**, 448–452 (2012).
- Kim, K. et al. Large-scale chirality in an active layer of microtubules and kinesin motor proteins. *Soft Matter* **14**, 3221–3231 (2018).
- Jung, W. et al. Collective and contractile filament motions in the myosin motility assay. *Soft Matter* **16**, 1548–1559 (2020).
- Zhou, H. et al. Durability of aligned microtubules dependent on persistence length determines phase transition and pattern formation in collective motion. *ACS Nano* **16**, 14765–14778 (2022).
- Barakat, J. M. et al. Surface topography induces and orients nematic swarms of active filaments: considerations for lab-on-a-Chip devices. *ACS Appl. Nano Mater.* **7**, 12142–12152 (2024).
- Hiratsuka, Y., Tada, T., Oiwa, K., Kanayama, T. & Uyeda, T. Controlling the direction of kinesin-driven microtubule movements along microlithographic tracks. *Biophys. J.* **81**, 1555–1561 (2001).
- Isele-Holder, R. E., Elgeti, J. & Gompper, G. Self-propelled worm-like filaments: Spontaneous spiral formation, structure, and dynamics. *Soft Matter* **11**, 7181–7190 (2015).
- Hess, H., Clemmens, J., Qin, D., Howard, J. & Vogel, V. Light-controlled molecular shuttles made from motor proteins carrying cargo on engineered surfaces. *Nano Lett.* **1**, 235–239 (2001).
- Bakewell, D. J. G. & Nicolau, D. V. Protein linear molecular motor-powered nanodevices. *Aust. J. Chem.* **60**, 314–332 (2007).
- Bachand, G. D., Bouxsein, N. F., Vandelinder, V. & Bachand, M. Biomolecular motors in nanoscale materials, devices, and systems. *Wiley Interdiscip. Rev. Nanomed. Nanobiotechnol.* **6**, 163–177 (2014).
- Saper, G. & Hess, H. Synthetic systems powered by biological molecular motors. *Chem. Rev.* **120**, 288–309 (2020).
- Kawamura, R. Integration of nanometric motor proteins towards a macroscopic power tool. *Jpn. J. Appl. Phys.* **62**, SG0807 (2023).
- Månsson, A. The potential of myosin and actin in nanobiotechnology. *J. Cell. Sci.* **136**, jcs261025 (2023).
- Lin, C. T., Kao, M. T., Kurabayashi, K. & Meyhofer, E. Self-contained, biomolecular motor-driven protein sorting and concentrating in an ultrasensitive microfluidic chip. *Nano Lett.* **8**, 1041–1046 (2008).
- Fischer, T., Agarwal, A. & Hess, H. A smart dust biosensor powered by kinesin motors. *Nat. Nanotechnol.* **4**, 162–166 (2009).
- Katira, P. & Hess, H. Two-stage capture employing active transport enables sensitive and fast biosensors. *Nano Lett.* **10**, 567–572 (2010).
- Korten, T., Månsson, A. & Diez, S. Towards the application of cytoskeletal motor proteins in molecular detection and diagnostic devices. *Curr. Opin. Biotechnol.* **21**, 477–488 (2010).
- Lard, M. et al. Ultrafast molecular motor driven nanoseparation and biosensing. *Biosens. Bioelectron.* **48**, 145–152 (2013).
- Nitta, T. & Hess, H. Effect of path persistence length of molecular shuttles on two-stage analyte capture in biosensors. *Cell. Mol. Bioeng.* **6**, 109–115 (2013).
- Isozaki, N. et al. Control of molecular shuttles by designing electrical and mechanical properties of microtubules. *Sci. Robot.* **2**, eaa4882 (2017).
- Kang'iri, S. M., Salem, A., Nicolau, D. V. & Nitta, T. Effects of defective motors on the active transport in biosensors powered by biomolecular motors. *Biosens. Bioelectron.* **203**, 114011 (2022).
- Kekic, M. et al. Biosensing using antibody-modulated motility of actin filaments on myosin-coated surfaces. *Biosens. Bioelectron.* **246**, 115879 (2024).
- Melbacke, A., Salhotra, A., Ušaj, M. & Månsson, A. Improved longevity of actomyosin in vitro motility assays for sustainable lab-on-a-chip applications. *Sci. Rep.* **14**, 22768 (2024).
- Nicolau, D. V. et al. Parallel computation with molecular-motor-propelled agents in nanofabricated networks. *Proc. Natl. Acad. Sci. U S A*. **113**, 2591–2596 (2016).
- Saper, G., Tsitkov, S., Katira, P. & Hess, H. Robotic end-to-end fusion of microtubules powered by kinesin. *Sci. Robot.* **6**, eabj7200 (2021).
- Akter, M. et al. Cooperative cargo transportation by a swarm of molecular machines. *Sci. Robot.* **7**, eabm0677 (2022).
- Sekimoto, K., Mori, N., Tawada, K. & Toyoshima, Y. Y. Symmetry breaking instabilities of an in vitro biological system. *Phys. Rev. Lett.* **75**, 172–175 (1995).
- Chelakkot, R., Gopinath, A., Mahadevan, L. & Hagan, M. F. Flagellar dynamics of a connected chain of active, polar, brownian particles. *J. R. Soc. Interface* **11**, 20130884 (2014).
- Vilfan, A., Subramani, S., Bodenschatz, E., Golestanian, R. & Guido, I. Flagella-like beating of a single microtubule. *Nano Lett.* **19**, 3359–3363 (2019).
- Fily, Y., Subramanian, P., Schneider, T. M., Chelakkot, R. & Gopinath, A. Buckling instabilities and spatio-temporal dynamics of active elastic filaments. *J. R. Soc. Interface* **17**, 20190794 (2020).
- Guido, I. et al. A synthetic minimal beating axoneme. *Small* **18**, e2107854 (2022).
- Yadav, S. A., Khatri, D., Soni, A., Khetan, N. & Athale, C. A. Wave-like oscillations of clamped microtubules driven by collective dynein transport. *Biophys. J.* **123**, 509–524 (2024).
- Bourdieu, L. et al. Spiral defects in motility assays: A measure of motor protein force. *Phys. Rev. Lett.* **75**, 176–179 (1995).
- Wang, C. et al. Conformation and dynamics of a tethered active polymer chain. *Phys. Rev. E*. **106**, 054501 (2022).
- Nitta, T. et al. Comparing guiding track requirements for myosin- and kinesin-powered molecular shuttles. *Nano Lett.* **8**, 2305–2309 (2008).
- Tsitkov, S. et al. The rate of microtubule breaking increases exponentially with curvature. *Sci. Rep.* **12**, 20899 (2022).
- Slater, B., Jung, W. & Kim, T. Emergence of diverse patterns driven by molecular motors in the motility assay. *Cytoskeleton* **81**, 902–912 (2024).
- Brangwynne, C. P. et al. Microtubules can bear enhanced compressive loads in living cells because of lateral reinforcement. *J. Cell Biol.* **173**, 733–741 (2006).
- Jin, M. Z. & Ru, C. Q. Localized buckling of a microtubule surrounded by randomly distributed cross linkers. *Phys. Rev. E* **88**, 012701 (2013).
- Kabir, A. M. R. et al. Buckling of microtubules on a 2D elastic medium. *Sci. Rep.* **5**, 17222 (2015).
- Afrin, T., Kabir, A. M. R., Sada, K., Kakugo, A. & Nitta, T. Buckling of microtubules on elastic media via breakable bonds. *Biochem. Biophys. Res. Commun.* **480**, 132–138 (2016).
- Ishigure, Y. & Nitta, T. Understanding the guiding of kinesin/microtubule-based microtransporters in microfabricated tracks. *Langmuir* **30**, 12089–12096 (2014).

51. Sweet, M., Kang'iri, S. M. & Nitta, T. Linking path and filament persistence lengths of microtubules gliding over kinesin. *Sci. Rep.* **12**, 3081 (2022).
52. Gittes, F., Mickey, B., Nettleton, J. & Howard, J. Flexural rigidity of microtubules and actin filaments measured from thermal fluctuations in shape. *J. Cell. Biol.* **120**, 923–934 (1993).
53. Rupp, B. & Nédélec, F. Patterns of molecular motors that guide and sort filaments. *Lab. Chip* **12**, 4903–4910 (2012).
54. Yildiz, A. Mechanism and regulation of kinesin motors. *Nat. Rev. Mol. Cell. Biol.* **26**, 86–103 (2025).
55. Kawaguchi, K. & Ishiwata, S. Nucleotide-dependent single- to double-headed binding of kinesin. *Science* **291**, 667–669 (2001).
56. Broedersz, C. P. & Mackintosh, F. C. Modeling semiflexible polymer networks. *Rev. Mod. Phys.* **86**, 995–1036 (2014).
57. Duke, T., Holy, T. E. & Leibler, S. “Gliding assays” for motor proteins: A theoretical analysis. *Phys. Rev. Lett.* **74**, 330–333 (1995).
58. Kraikivski, P., Lipowsky, R. & Kierfeld, J. Enhanced ordering of interacting filaments by molecular motors. *Phys. Rev. Lett.* **96**, 258103 (2006).
59. Palacci, H. et al. Velocity fluctuations in kinesin-1 gliding motility assays originate in motor attachment geometry variations. *Langmuir* **32**, 7943–7950 (2016).
60. Nédélec, F. & Foethke, D. Collective Langevin dynamics of flexible cytoskeletal fibers. *New J. Phys.* **9**, 427 (2007).
61. Hirokawa, N. Kinesin and dynein superfamily proteins and the mechanism of organelle transport. *Science* **279**, 519–526 (1998).
62. Gibbons, F., Chauwin, J. F., Despósito, M. & José, J. A dynamical model of kinesin-microtubule motility assays. *Biophys. J.* **80**, 2515–2526 (2001).

Acknowledgements

This work was supported by JSPS KAKENHI 22H04951 and 23K22714 to T.N. and NSF Grant 2230116 to H.H. D.K.N. thanks Amano Institute of Technology and THERS Make New Standards Program for their scholarships.

Author contributions

D.K.N., H.H. and T.N. conceived and designed this work. D.K.N. performed the simulations. D.K.N. and T.N. performed the data analysis. All authors contributed to interpretation and writing the paper. All authors have given approval to the final version of the manuscript.

Declarations

Competing interests

The authors declare no competing interests.

Additional information

Supplementary Information The online version contains supplementary material available at <https://doi.org/10.1038/s41598-025-03384-y>.

Correspondence and requests for materials should be addressed to T.N.

Reprints and permissions information is available at www.nature.com/reprints.

Publisher's note Springer Nature remains neutral with regard to jurisdictional claims in published maps and institutional affiliations.

Open Access This article is licensed under a Creative Commons Attribution-NonCommercial-NoDerivatives 4.0 International License, which permits any non-commercial use, sharing, distribution and reproduction in any medium or format, as long as you give appropriate credit to the original author(s) and the source, provide a link to the Creative Commons licence, and indicate if you modified the licensed material. You do not have permission under this licence to share adapted material derived from this article or parts of it. The images or other third party material in this article are included in the article's Creative Commons licence, unless indicated otherwise in a credit line to the material. If material is not included in the article's Creative Commons licence and your intended use is not permitted by statutory regulation or exceeds the permitted use, you will need to obtain permission directly from the copyright holder. To view a copy of this licence, visit <http://creativecommons.org/licenses/by-nc-nd/4.0/>.

© The Author(s) 2025